Orthogonal Load-Modulated Balanced Amplifier for Back-Off Efficiency Enhancement and Agile Frequency Configuration

Jean-Baptiste Urvoy, *Student Member, IEEE,* Ehsan M. Azad, *Member, IEEE,* Aleksander Bogusz, *Member, IEEE,* Steve C. Cripps, *Life Fellow, IEEE* and Roberto Quaglia, *Member, IEEE,*

***Abstract*—This paper presents the theory of operation and the design guidelines for an orthogonal load-modulated balanced amplifier with back-off efficiency enhancement. The single-input balanced amplifier is operated by asymmetrically biasing the devices, similarly to a Doherty configuration, where the main amplifier operates in class AB and the auxiliary in class C. The paper shows how the reflective termination at the output isolated port, a key element of the orthogonal load modulated balanced amplifier, can compensate for the non-null phase delay of the output matching network. This means the operational frequency can be optimized electronically by controlling the reflective termination at the output isolated port. At the same time, the matching network design can focus on the maximum power case without phase delay constraints. The paper also quantifies the impact of losses in the electronically configurable elements and the power handling requirements. The theory is validated with the design, simulation, and experimental characterization of a prototype based on GaN active devices. The tunable reflective termination is achieved through an RF single-pole, four-throw switch that switches between fixed reflective loads. The measurements on the prototype compare well with the state-of-the-art. When tested on the 0.8–1.6 GHz octave bandwidth, the single-tone maximum output power is between 45 and 47.3 dBm, and the 6-dB back-off efficiency is better than 48%. The system-level measurements using a 5 MHz channel signal with 6-dB crest factor show, at different carrier frequencies across the band, an average output power between 40 and 42 dBm, an efficiency better than 41%, and the linearizability of the prototype to meet spectral distortion requirements.**

***Index Terms*—Balanced amplifier, Doherty power amplifier, efficiency enhancement, gallium nitride, power amplifier.**

I. Introduction

THERE is an increased interest in high-frequency transmitters that can operate at high power efficiency in multiple configurations that can be selected electronically, effectively enabling a software-controlled transmitter or the reuse of the same PA in different radios [1]. This creates new challenges for the Power Amplifier (PA) design, which must target several contrasting performance metrics, including high linearity, high efficiency, average power adjustment, and broadband or configurable operation.

The Doherty PA has proven the most successful solution for improving the trade-off between linearity and power efficiency [2], [3]. However, increasing the bandwidth of a Doherty design is difficult as, to achieve the required load modulation, the phase response of the matching networks [4] and the impedance inverter [5] must be kept under tight control over the design bandwidth. Nonetheless, there are many examples of Doherty designs with significant RF bandwidth. Most of them focus on the design of the output combiner first, trying to minimize phase dispersion by employing different techniques of matching and impedance inversion [6]–[10].

Doherty PAs with tunable center frequency have also been proposed. For example, micro-eletromechanical system (MEMS) switches were used in [11] to tune the response of the Doherty combiner and achieved the configuration of the operation frequency at 1.9, 2.14 and 2.6 GHz. In [12], the phase periodicity of the matching networks of a Doherty PA was exploited to exchange the role of main and auxiliary PAs at different frequencies, by adjusting the gate bias of the two stages, and controlling the operation frequency between 1.52 and 4.68 GHz.

The Load Modulated Balanced Amplifier (LMBA) was introduced as a flexible load modulation architecture that allowed optimization vs frequency [13], as well as improved back-off efficiency [14]–[16]. In the LMBA, the phase of the matching networks is not critical for the load modulation, as it can be compensated for by controlling the input phase difference between main (balanced) and auxiliary (control signal power, CSP) signals. However, intrinsic to its mode of operation, the LMBA used this way is non-linear and with a limited output back-off (OBO) region [14]. Derived from the LMBA - but with the balanced amplifier playing the role of auxiliary PA - the sequential, or inverted, LMBA has led to much improved back-off extension, offering linear operation [17], [18]. Record bandwidths and efficiencies have been presented using this solution or its variations [19], [20].

This paper proposes an alternative solution for a frequency-agile PA with a high-efficiency back-off region. The architecture is derived from the Orthogonal LMBA (OLMBA) structure. Compared to LMBA, in OLMBA, the CSP signal is injected at the input coupler rather than the output, and a reflective termination is used at the output coupler isolated

Manuscript received XX; YY, ZZ.

This paper is an expanded version from the International Workshop on Nonlinear Microwave and Millimetre-Wave Circuits, Torino, Italy, April 10-11, 2015

The authors would like to acknowledge the project EP/Z533828/1 MUST-RF funded by the Engineering and Physical Sciences Research Council (EPSRC).

J.-B. Urvoy, A. Bogusz, S.C. Cripps and R. Quaglia are with the Centre for High Frequency Engineering, Cardiff University, Queens' Buildings, The Parade, CF24 3AA, Cardiff, UK e-mail: quagliar@cardiff.ac.uk

E.M. Azad is with the Compound Semiconductor Applications Catapult, Celtic Technology Centre, Celtic Way, Newport, NP10 8BE, UK

port to control the load modulation alongside the CSP signal. The OLMBA was originally proposed as a frequency agile technique for peak power operation [21] and load mismatch mitigation [22]. It was found experimentally that by biasing one of the balanced devices in class C, efficiency enhancement in back-off was possible, and that the reflective termination could be used to tune the frequency of operation [23]. However, the results showed only moderate efficiency enhancement due to the fact that the design originally targeted frequency tuning only, not back-off efficiency enhancement. Following on that work, the design and simulations presented in [24] showed a computer-aided design (CAD) based approach to a Doherty-like OLMBA, where the matching networks were tuned for peak power operation, and the reflective termination could be optimized using a swept variable in CAD. This paper, an extension of the conference paper [24], explains, for the first time, the underlying mechanism for Doherty-like operation of the architecture, also allowing us to derive a recipe for the design and an understanding of its limitations. Also, in addition to the conference paper where simulations only were reported, this paper presents a finalized design of a prototype with a comprehensive experimental characterization.

The design introduced in this paper can also be seen as a Doherty PA with a quadrature coupler used as an impedance inverter, which is not new [25]. However, using a coupler does not directly give a bandwidth advantage compared to a standard transmission line inverter, as the dominant band-limiting factor is the phase response of the devices' reactive effects and matching networks, rather than the inverter itself. The novelty of this paper is that it uses the reflective termination, typical of the OLMBA, to compensate for the matching network delay, which leads to broadband Doherty-like load modulation in principle. The key difference between the work presented in [22] and this work is the desired outcome of the two works. [22] focuses on using the OLMBA as a method to mitigate the effects of load mismatch, while this paper will endeavour to present the OLMBA as a method for wideband reconfigurable, focusing on enhancing OBO efficiency. Furthermore, this work exploits a similar output combiner as in [25], however, by using a reactive termination on the output isolate port of the device it is able to be reconfigured to be operational over a wider bandwidth. The use of a tunable reflective termination in a coupler-based Doherty was also explored in [26], not for frequency configuration, but in a narrow-band design to control the phase conversion profile and improve linearity.

The paper is organized as follows: Section II describes, with simplified models, the theory of operation of the proposed PA architecture. Section III focuses on the tunable termination by discussing the effect of its losses and deriving a first approximation of the voltage/current it must handle. Section IV and V describe the design and characterization of the prototype, respectively, while Section VI will draw some conclusions.

II. Principle of Operation

Fig. 1 shows the basic circuit diagram of the proposed PA, which is based on an OLMBA configuration, with a reflective termination Γ_x at the output coupler isolated port, but with a single RF input. The signal at the Γ_x port derives from biasing one of the two transistors in class AB, and the other in class C, effectively unbalancing the balanced PA at low drive level.

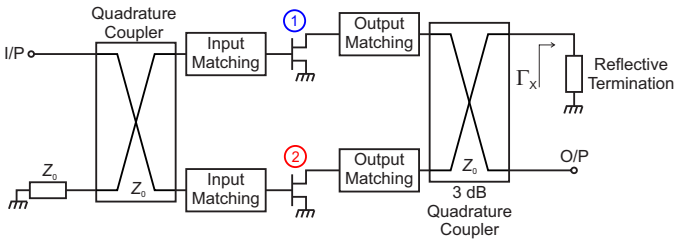

Fig. 1. Basic circuit diagram of the proposed amplifier.

The circuit analysis starts from the output section, see Fig. 2, where the equivalent reactive effects at the output of the active devices, the output matching network, and the internal delays of the coupler are grouped in 2-port networks, identical for the two balanced branches. In an ideal case, these 2-port networks are lossless and, at each design frequency, transform the coupler impedance Z_0 into the optimum intrinsic load of the device $R_{\rm opt}$, with an arbitrary equivalent phase delay $\Delta\Phi$ (the delay of a physical transmission line is here defined as a positive value, i.e., a microstrip line with phase of $S_{21} = -\pi/4$ means $\Delta\Phi = \pi/4$). In this Section, it will be demonstrated that by setting the proper phase of Γ_x, a Doherty-like behavior of the amplifier can be achieved.

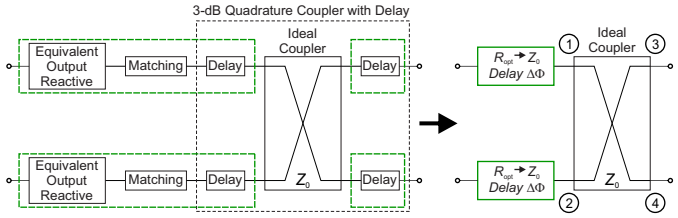

Fig. 2. Transformation of the output section of the balanced amplifier to an equivalent with an ideal coupler and grouped 2-port networks.

The next, less obvious, step is to connect, at ports 3 and 4 of the couplers, a hypothetical delay line of the same impedance of the coupler Z_0, and phase delay that is $-\Delta\Phi$. By doing so, the overall 4-port network is now a "matching" coupler, i.e., an ideal, lossless 3-dB quadrature coupler where the port impedance is $R_{\rm opt}$ for port 1 and 2, and Z_0 for port 3 and 4, see Fig. 3 and the derivation in Appendix A.

The output section can be now represented as in Fig. 4, where active devices are modeled as ideal current sources, the output is matched to Z_0, and an impedance $Z_{\rm h}$ is connected at port 3, which will be the reflective termination.

The coupler $\mathbf{Z}$ matrix can be written as

$$\mathbf{Z} = -jZ_0 \begin{bmatrix} 0 & r_{\rm opt} & 0 & \sqrt{2r_{\rm opt}} \\ r_{\rm opt} & 0 & \sqrt{2r_{\rm opt}} & 0 \\ 0 & \sqrt{2r_{\rm opt}} & 0 & 1 \\ \sqrt{2r_{\rm opt}} & 0 & 1 & 0 \end{bmatrix}, \quad (1)$$

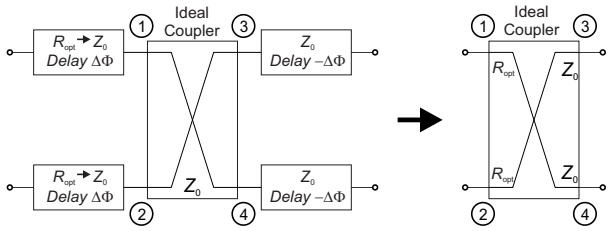

Fig. 3. Ideal coupler with impedance Z_0, loaded with ideal matching on ports 1, 2, and hypothetical delay lines on ports 3, 4, can be transformed into an ideal "matching" coupler with different port impedance at ports 1, 2 and 3, 4.

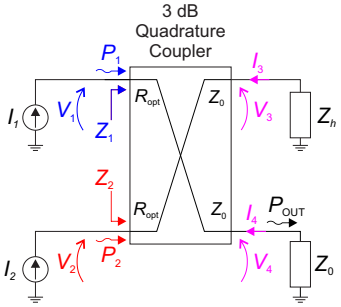

Fig. 4. Simplified output section of the proposed PA.

where $r_{\mathrm{ropt}} = R_{\mathrm{opt}}/Z_0$. The boundary conditions are:

$$\begin{cases} V_3 = -Z_{\mathrm{h}} I_3 = -Z_0 z_{\mathrm{h}} I_3 = -\frac{Z_0}{y_{\mathrm{h}}} I_3 \\ V_4 = -Z_0 I_4 \end{cases} \tag{2}$$

where z_{h} and y_{h} are the normalized reflective impedance and admittance, respectively. These mean that we can write the currents at ports 3 and 4 as:

$$\begin{cases} I_3 = \quad jy_{\mathrm{h}}\sqrt{2r_{\mathrm{opt}}} I_2 \quad + jy_{\mathrm{h}} I_4 \\ I_4 = \quad j\sqrt{2r_{\mathrm{opt}}} I_1 \quad\quad + jI_3 \end{cases}, \tag{3}$$

and then solve in terms of the current at port 1 and 2 as:

$$\begin{cases} I_3 = \quad -\sqrt{2r_{\mathrm{opt}}}\frac{y_{\mathrm{h}}}{1+y_{\mathrm{h}}} I_1 \quad + j\sqrt{2r_{\mathrm{opt}}}\frac{y_{\mathrm{h}}}{1+y_{\mathrm{h}}} I_2 \\ I_4 = \quad j\sqrt{2r_{\mathrm{opt}}}\frac{1}{1+y_{\mathrm{h}}} I_1 \quad - \sqrt{2r_{\mathrm{opt}}}\frac{y_{\mathrm{h}}}{1+y_{\mathrm{h}}} I_2 \end{cases}. \tag{4}$$

These can be inserted in the equations for the voltage at port 1 and 2:

$$\begin{cases} \frac{V_1}{R_{\mathrm{opt}}} = \quad \frac{2}{1+y_{\mathrm{h}}} I_1 \quad - j\frac{1-y_{\mathrm{h}}}{1+y_{\mathrm{h}}} I_2 \\ \frac{V_2}{R_{\mathrm{opt}}} = \quad -j\frac{1-y_{\mathrm{h}}}{1+y_{\mathrm{h}}} I_1 \quad + 2\frac{y_{\mathrm{h}}}{1+y_{\mathrm{h}}} I_2 \end{cases}. \tag{5}$$

If we represent the reflective load in terms of reflection coefficient Γ_{h} normalized to Z_0, we have:

$$y_{\mathrm{h}} = \frac{1-\Gamma_{\mathrm{h}}}{1+\Gamma_{\mathrm{h}}}, \tag{6}$$

that can be substituted in (5):

$$\begin{cases} \frac{V_1}{Z_0} = \quad (1+\Gamma_{\mathrm{h}})\, I_1 \quad\quad -j\Gamma_{\mathrm{h}} I_2 \\ \frac{V_2}{Z_0} = \quad -j\Gamma_{\mathrm{h}} I_1 \quad + (1-\Gamma_{\mathrm{h}})\, I_2 \end{cases}. \tag{7}$$

It is possible now to set the current sources as:

$$I_2 = -j\alpha I_1, \tag{8}$$

which allows to substitute in (5) to calculate the impedance at the ports by then dividing each voltage at the ports by the corresponding current:

$$\begin{cases} Z_1 = R_{\mathrm{opt}}\left(1 + \Gamma_{\mathrm{h}} - \alpha\Gamma_{\mathrm{h}}\right) \\ Z_2 = R_{\mathrm{opt}}\left(1 - \Gamma_{\mathrm{h}} + \frac{1}{\alpha}\Gamma_{\mathrm{h}}\right) \end{cases}. \tag{9}$$

The balanced case is for $\alpha = 1$, which means that $Z_1 = Z_2 = R_{\mathrm{opt}}$, consistently with how the balanced PA works, and it represents the full power case where both devices are delivering the maximum power.

Similarly, as in a Doherty PA, we can set one of the devices to play the role of the Auxiliary device, and be turned off for input drive lower than a certain level. If we assume the current source I_1 represents the Main device, then we can set $\alpha = 0$ to check the impedance at back-off.

This means:

$$\begin{cases} Z_{1,\mathrm{OBO}} = R_{\mathrm{opt}}\left(1 + \Gamma_{\mathrm{h}}\right) \\ Z_{2,\mathrm{OBO}} \to R_{\mathrm{opt}}\left(\frac{1}{\alpha}\Gamma_{\mathrm{h}}\right) \end{cases} \tag{10}$$

To replicate a conventional 6-dB Doherty behavior, where the impedance at back-off should be doubled and the break-point is at half the maximum drive, it is then sufficient to set $\Gamma_{\mathrm{h}} = 1$, which is an open circuit, to obtain $Z_1 = 2Z_0$. This also means the auxiliary device will see an open circuit ($Z_2 = +\infty$).

Also, it can be noted that the output current can be re-written as:

$$I_4 = j\sqrt{2} I_1 \frac{1+\alpha y_{\mathrm{h}}}{1+y_{\mathrm{h}}} = \frac{jI_1}{\sqrt{2}}\left[1 + \Gamma_{\mathrm{h}} + \alpha\left(1 - \Gamma_{\mathrm{h}}\right)\right] \tag{11}$$

which means that for reflective termination at open circuit ($\Gamma_{\mathrm{h}} = 1$), the output current only depends on the main current:

$$I_4 = j\sqrt{2} I_1. \tag{12}$$

Hence, the proposed amplifier is linear if the main amplifier is linear.

It is also easy to demonstrate that by inverting the role of the main and the auxiliary, and using a short circuit at Γ_{h}, the same behavior is achieved.

So, the proposed structure, with an open circuit at port 3 will operate as an ideal Doherty over the bandwidth of the coupler itself. In this paper, only the case with the same devices for the main and auxiliary PAs is considered, for a 6-dB OBO design.

To revert this hypothetical structure to a realistic amplifier, we can remove the delay line at port 4, as it is a Z_0 line loaded with Z_0. Then, we can substitute the cascade of the delay line and the open circuit with a reflective termination with a reflection coefficient angle that is $2\Delta\Phi$, see Fig. 5.

The final result is that, at each frequency where the output matching network provides accurate impedance transformation, and the 3-dB coupler is in band, we can compensate for the non-null phase of the matching networks and achieve an ideal Doherty-like behavior by selecting

$$\Gamma_{\mathrm{x}} = e^{2j(\Delta\Phi + n\pi)}, \tag{13}$$

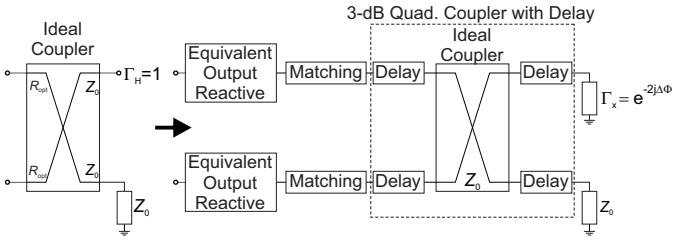

Fig. 5. The ideal matching coupler used as the output section of the coupler-based Doherty PA, with open circuit at port 3, reverted to a realizable structure with reflective termination with defined phase at port 3.

where n is an integer.

III. Considerations about Reflective Termination

The phase response vs frequency of the reflective termination is not trivial. The phase delay $\Delta\Phi$ will most likely correspond to a positive group delay if low-loss broadband matching is used in the output matching network. This means that the reflective termination will require a non-trivial phase response, which can be achieved using negative group delay networks, but with a significant trade-off between bandwidth and losses. Therefore, this paper focuses on a reconfigurable reflective termination, where the value of Γ_x is tuned electronically when the frequency of operation is changed, offering agile frequency configuration of the hardware.

Loss in the reflective termination can still be significant with configurable elements such as varactors or switches, so it is helpful to quantify the impact of these losses on the PA performance. Let's consider again the structure of Fig. 4 with Γ_h, as it can be related to Γ_x with a simple phase rotation. The reflective termination must be an open circuit to achieve the correct Doherty-like behavior. The case with losses means that:

$$\Re\{\Gamma_h\} = |\Gamma_h| = \Gamma_h < 1, \tag{14}$$

Let's observe the main impedance, which is:

$$Z_1 = Z_0\left(1 + \Gamma_h - \alpha\Gamma_h\right). \tag{15}$$

and the output current, which is:

$$|I_4| = \frac{1}{\sqrt{2}} I_1\left[1 + \Gamma_h + \alpha\left(1 - \Gamma_h\right)\right] \tag{16}$$

At full power ($\alpha = 1$), we have:

$$\begin{cases} Z_{1,\mathrm{SAT}} = Z_0\left(1 + \Gamma_h - \Gamma_h\right) = Z_0 \\ |I_4| = \frac{1}{\sqrt{2}} I_1\left[1 + \Gamma_h + \left(1 - \Gamma_h\right)\right] = \sqrt{2} I_1 \end{cases}, \tag{17}$$

meaning that, at saturation, the loss in the reflective termination does not affect the device impedance or the output power. At back-off ($\alpha = 0$), we have:

$$\begin{cases} Z_{1,\mathrm{SAT}} = Z_0\left(1 + \Gamma_h\right) < 2Z_0 \\ |I_4| = \frac{1}{\sqrt{2}} I_1\left(1 + \Gamma_h\right) < \sqrt{2} I_1 \end{cases}, \tag{18}$$

which means output power and efficiency are both reduced at back-off, with a negative impact on efficiency. Assuming ideal class B waveforms for both devices, the RF current for the main is:

$$I_1 = \frac{1}{2}\beta I_{\mathrm{MAX}}, \tag{19}$$

where β is a sweep parameter from 0 to 1, representing the input drive, and I_{MAX} is the maximum device current. For the auxiliary, the RF current is

$$\begin{cases} I_2 = 0 & 0 \le \beta < \frac{1}{2} \\ I_2 = -j\frac{1}{2}(2\beta - 1) I_{\mathrm{MAX}} & \frac{1}{2} \le \beta \le 1 \end{cases} \tag{20}$$

For both devices, the DC currents can be calculated from the RF currents by scaling by a factor $2/\pi$. The RF voltage at the ports can be evaluated by multiplying the currents by the impedances of (5), while the DC voltage is set constant at the DC voltage V_{MAX} that avoids clipping at maximum drive:

$$V_{\mathrm{MAX}} = \frac{1}{2} I_{\mathrm{MAX}} Z_0 \tag{21}$$

With these variables, the normalized output power and the efficiency can be calculated and plotted, see Fig. 6, for different values of loss in the reflective termination. The output power

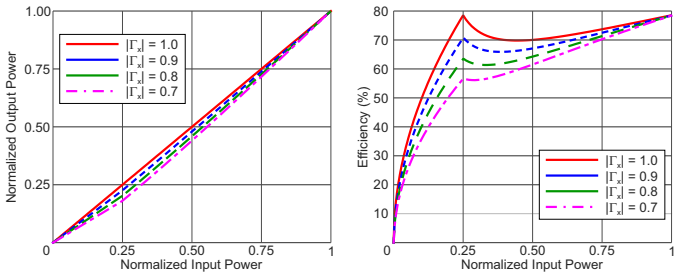

Fig. 6. Effect of loss in reflective termination on the performance of ideal Doherty-like OLMBA. Normalized output power (left) and efficiency (right) vs. normalized input power.

is affected at most at the break-point, meaning that the gain is also distorted.

Another important consideration when introducing tunable elements is their power handling. As the tunable elements are inserted to produce a reflective termination, in principle, the true power to be handled is zero, or relatively small in case of losses. In contrast, large reactive power will be present. Hence, the limiting factor for the tunable components is not power, but voltage or current applied to them, which might lead to unwanted distortion or even the failure of the components. Also in this case, we refer to the schematic of Fig. 4, where the voltage at the open circuit V_3 is the parameter to observe. The voltage at the port can be expressed as:

$$V_3 = \frac{Z_0}{\sqrt{2}}\left(1 + \Gamma_h\right)\left(I_1 - jI_2\right) \tag{22}$$

which, by applying the current profiles discussed earlier and assuming an open-circuit termination, is:

$$\begin{cases} V_3 = \frac{Z_0}{\sqrt{2}}\beta I_{\mathrm{MAX}} & 0 \le \beta < \frac{1}{2} \\ V_3 = \frac{Z_0}{\sqrt{2}}\left(1 - \beta\right) I_{\mathrm{MAX}} & \frac{1}{2} \le \beta \le 1 \end{cases} \tag{23}$$

For a more general result, it is more useful to normalize the result to the maximum output power rather than the device current. The maximum output power is:

$$P_{\mathrm{MAX}} = \frac{1}{2} Z_0 |j \frac{1}{\sqrt{2}} I_{\mathrm{MAX}}|^2 = \frac{1}{4} Z_0 I_{\mathrm{MAX}}^2 \tag{24}$$

Hence, we can rewrite V_3 as:

$$\begin{cases} V_3 = \beta \sqrt{2 Z_0 P_{\mathrm{MAX}}} & 0 \leq \beta < \frac{1}{2} \\ V_3 = (1-\beta) \sqrt{2 Z_0 P_{\mathrm{MAX}}} & \frac{1}{2} \leq \beta \leq 1 \end{cases} \tag{25}$$

The profile of the normalized $|V_3|$ is shown in Fig. 7, highlighting how that the maximum voltage

$$\max\{|V_3|\} = \sqrt{\frac{Z_0 P_{\mathrm{MAX}}}{2}} \tag{26}$$

is applied at the break point ($\beta = 0.5$), while it decreases to zero at saturation where the balanced structure isolates port 3.

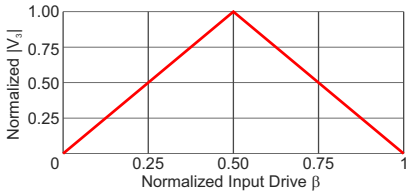

Fig. 7. Normalized $|V_3|$ vs. input drive β.

For the actual amplifier topology, the maximum of the voltage V_{x} and current I_{x} at the "real" reflective termination Γ_{x} can be expressed as:

$$\begin{cases} \max\{|V_{\mathrm{x}}|\} = \sqrt{\frac{Z_0 P_{\mathrm{MAX}}}{2}} \left|\cos(-\Delta\Phi)\right| \\ \max\{|I_{\mathrm{x}}|\} = \sqrt{\frac{P_{\mathrm{MAX}}}{2 Z_0}} \left|\sin(-\Delta\Phi)\right| \end{cases} \tag{27}$$

This also means:

$$P_{\mathrm{MAX}} = 2 \left[\frac{1}{Z_0} \left(\max\{|V_{\mathrm{x}}|\}\right)^2 + Z_0 \left(\max\{|I_{\mathrm{x}}|\}\right)^2 \right]. \tag{28}$$

The equations presented in this section can help obtain the first approximation of the impact of loss and the voltage/current handling of the reflective termination. CAD simulations can be used later in the design process for fine-tuning and verification of these effects. If large signal models of the reflective termination or its components are available, the contribution to distortion can also be evaluated.

IV. Prototype Design

A. Design Procedure

The proposed design procedure for the new OLMBA can be summarized as follows:

1) Select active device and determine an equivalent model of the output, in class AB and class C.
2) Design matching networks for optimum power over the frequency band of interest, matched to the coupler impedance.
3) If the class AB and C models are different, make sure the cascade of the output model and the matching network have equalized phase delays between the two stages.
4) Stabilize and match the input of the devices.
5) Determine the optimum ideal values of Γ_{x}
6) Determine the optimum input splitting ratio and bias for targeted linear behavior.
7) Substitute ideal components with physical components.

The prototype was designed on the RO4053 substrate with the MACOM (former Wolfspeed) CG2H40025F as active devices. Load-pull analysis found that the optimum intrinsic impedance is at around 12 Ω. A negative series inductor and shunt capacitor were tuned on the device's output to find the optimum extrinsic parasitics to de-embed to maximize output power and maintain good drain efficiency across the full bandwidth. For the class AB amplifier, these values were found to be 2.8 pF and 0.35 nH; for the class C auxiliary amplifier, these were found to be 2.4 pF and 0.4 nH. The output matching networks were designed to match the optimum impedance of 12 Ω while de-embedding the necessary parasitics.

Maintaining a constant phase relationship between the main and auxiliary branches is crucial for the Doherty-like load modulation function. Thus, quarter-wave transformers were chosen as the matching strategy. This is because the performance of quarter-wave transformers is highly predictable and easy to simulate– especially in terms of the phase shift they provide. The number of sections chosen was three, as fewer than that did not provide a good enough match, and because of the linear relationship between the delay of the matching network and the phase of Γ_{x}, making the matching network too long could significantly reduce the instantaneous bandwidth when amplifying modulated signals. Once the matching networks were designed, it was found that there was a phase difference of around 6 degrees between the main and auxiliary branches, likely caused by the different transistor classes. As this phase difference was found to have minimal impact on the device performance it was decided not to compensate for it to avoid overcompensation in case the device model was inaccurate in class C.

Following the design of the stability network, which ensured small-signal broadband unconditional stability of each stage over a range of bias points, the input matching was done to ensure good input matching at saturation. The Γ_{x} was initially modeled as a 1-port S-parameter block with the magnitude of its reflection coefficient set to 1 (i.e., lossless) and a controllable phase. To find the optimum phase of Γ_{x} at each frequency point, the phase is swept in back off — input power is 0 dBm – and the optimum phase is where the intrinsic impedance is closest to twice the optimum impedance (24 Ω). Fig. 8 shows, as an example of the method used to identify the optimum at each frequency point, the intrinsic impedance of the main device at 1.2 GHz at OBO when the phase of Γ_{x} is swept; the point closest to 24 Ω is deemed the optimum.

With this procedure, the phase of Γ_{x} has been optimized with a CAD algorithm. However, the theory states in (13) that the optimum phase of Γ_{x} is twice the phase delay $\Delta\Phi$ of the cascade network of reactive effects and matching network. By plotting together the theoretical value and the one obtained

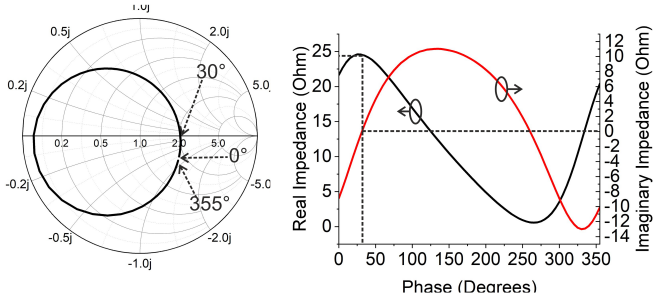

Fig. 8. a) Intrinsic impedance of the main device as the phase of Γ_x is swept. Smith chart normalized to 12 Ω b) real and imaginary parts of the intrinsic impedance of the main device as the phase of the reflection coefficient of Γ_x. The dashed line indicates where the intrinsic impedance is deemed optimum - 30-degrees.

solely through search in the swept simulation, this can be verified as shown in Fig. 9.

The next step is to select the power splitting on the input. Having even or uneven power splitting on the device's input has advantages and disadvantages. Even power splitting should make the design simpler. It would also allow switching between the main and auxiliary devices and provide more gain, as less power would be dissipated in the isolated port at back off. On the other hand, by having more power going to the auxiliary device, the auxiliary device will be able to consistently saturate at the same point as the main device, ensuring full use of the device in the 6-dB OBO region. As this device is intended to enhance OBO performance, uneven splitting was chosen to maximize the device's effectiveness in the OBO region.

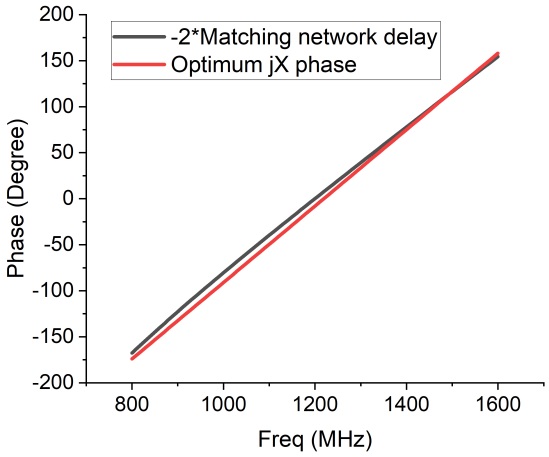

Fig. 9. Comparison of the delay of the output matching network and optimum phase of the reflection coefficient of Γ_x.

To find the optimum power splitting and optimum auxiliary gate voltage ADS's Hybrid90 device was used. This component is an ideal 90-degree hybrid coupler with a number of controllable parameters, the most important for these being Gain Balance between the two output ports. The Gain Balance and the auxiliary gate voltage can be swept along with the

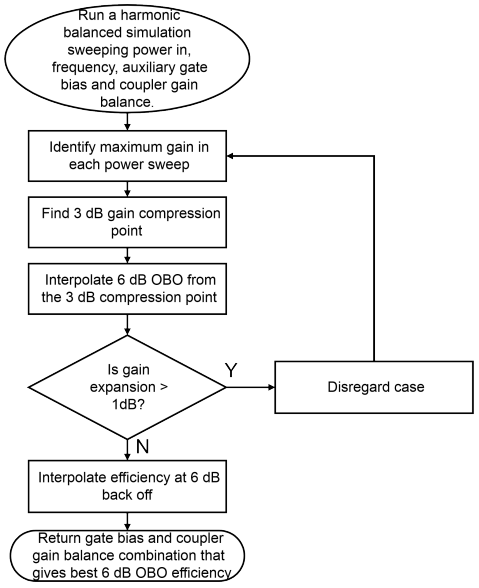

Fig. 10. Flowchart of the algorithm used to find optimum input power slitting and auxiliary gate bias for OBO efficiency optimization

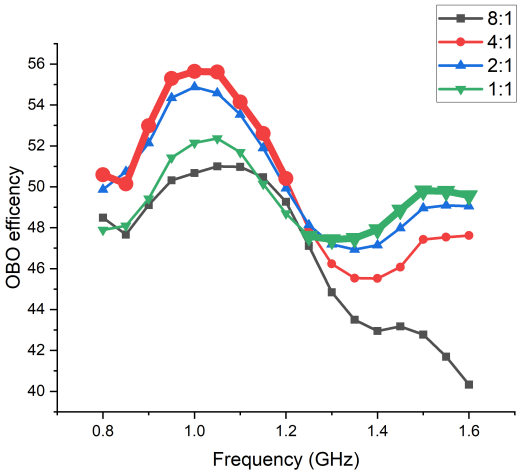

Fig. 11. Maximum OBO drain efficiency found by the MATLAB algorithm under different input power split ratios as the auxiliary gate voltage is swept. Legend reported as the ratio of power to the auxiliary device to the power to the main device. In bold are the optimal power spit ratios, 4:1 at the lower end of the frequency band and 1:1 at the upper end

input power at all frequency points. An algorithm was built in MATLAB to ascertain the optimum power splitting and auxiliary gate voltage combination. A flow diagram in Fig. 10 details how this algorithm finds the optima at each frequency point. In the flow chart, cases where gain expansion is too high are disregarded to make linearisation easier. Fig. 11 shows the algorithmically found optimum power splitting ratio on the input coupler to provide the best 6 dB OBO drain efficiency. It is found that the required power splitting is not the same across the frequency band, and that at the upper end of the band, a more even split is preferable, but at the lower end, more power to the auxiliary is required. This behavior is reminiscent of a hybrid coupler used out of its frequency

band. Running further sweeps of power, auxiliary gate bias and frequency with different couplers designed for 1.6–4 GHz, the 11036 coupler from Xinger provided the best OBO efficiency. Its forward transmission parameter and power split ratio are shown in Fig. 12. For the output, the IPP-7048 0.8-1.6 GHz hybrid coupler was chosen.

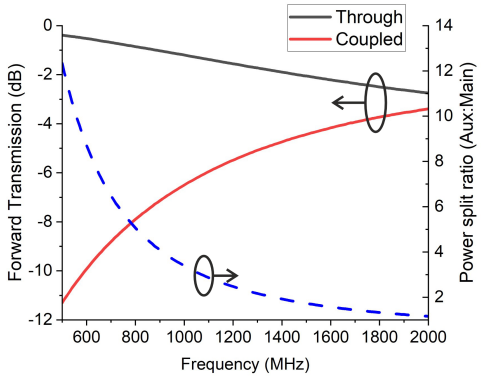

Fig. 12. Forward transmission parameters of Xinger-11036 hybrid coupler from input port to through and coupled ports. The ratio of power to the auxiliary device to the power to the main device is shown in the blue dashed trace. Touchstone data used is available on TTM technologies website

The ideal Γ_x has been shown to be inversely proportional to the delay of the matching networks. The issue is that to achieve this, the reflection coefficient of the Γ_x must go anticlockwise around the edge of the Smith chart while remaining lossless, which is not possible. Thus, several different reactive terminations that we can switch between are necessary. Previous OLMBA work has opted for CMOS switches with reactive loads to act as the Γ_x port. As this method had worked well previously, this solution was chosen for the new design as well.

Selecting the RF switch requires some important considerations. Firstly, it must be able to handle the power at 6 dB OBO and be low loss. In addition, the device should have as many terminations as possible to maximise the number of Γ_x phases available at each frequency point. Generally, there is a tradeoff between the number of RF switch terminations and both the power handling and insertion loss provided. Switches with more terminations tend to have a lower maximum input power and high insertion loss. On the other hand, switches with only two terminations typically have excellent power handling, but are far more limited in their use for this device. The ADRF5347 from Analog Devices was selected as it has relatively high power handling (39 dBm in CW conditions) while offering a good number of possible terminations – 4. It is worth noting that, as the switch is not in the direct output power path, it is not necessary for it to be able to sustain the whole power targeted, up to 46-47 dBm. Also, as the switch will not operate in a 50 Ω environment, but with a reflective termination, the actual response to the signal applied will need to be verified experimentally. In the interest of time, we were not able to perform a full large signal characterization of the switch, as done for example in [27], but the approach has been to take a risk and use the switch without a full characterization of signal handling with reflective terminations. As a mitigation, it was decided to limit the preliminary single-tone characterization to pulsed-RF only and apply a CW signal in the modulated case. The scattering parameters of the switch were measured, using the evaluation board provided by Analog Devices, to model the switch in ADS.

While a framework to predict the required Γ_x for load modulation has been demonstrated, there is some uncertainty in the phase delay of the switch and the coupler; thus, it was elected to select switch terminations based on what would provide maximal Smith chart coverage. i.e., the four reactive terminations should be around 90 degrees from each other around the edge of the Smith chart at center frequency. The first termination selected was an open circuit, then a small inductor and capacitor were tuned to provide ± 90-degree phase shift, then a large capacitor was added to approximate a short circuit. The selected components gave a starting point for what was needed in the hardware and the exact required values were found experimentally; the used terminations were: an open circuit; 2.4 pF (-j50 Ω); 4.7 nH (+j40 Ω); and 15 pH (low impedance, approximating a short circuit). The simulated Γ_x when using the switch with the reactive loads is shown in Fig. 14, both on Smith chart and as a phase plot vs. frequency. As shown, the reactive terminations cover most of the outside edge of the Smith chart and maintain a 90-degree phase relationship with each other. The mean magnitude of the four Γ_x states is 0.944; thus, the losses from the switch should be minimal. The theory laid out in Section III suggests that this would equate to a loss or around 5% OBO efficiency in a purely idealistic Doherty-like OLMBA device. It is important to note, however, that this is small signal loss and does not capture potential losses from the switch compressing at higher power levels.

B. Design Finalization and Simulations

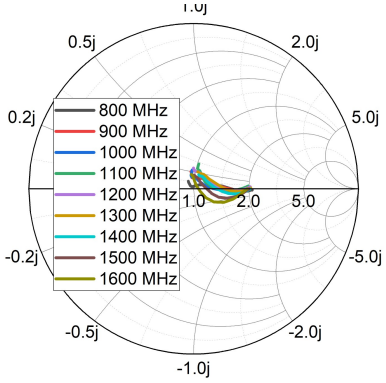

Fig. 13. Load trajectory with ideal Γ_x reflection coefficient phase. The chart is normalized to 12 Ω.

Simulations were initially run using the ideal Γ_x phase as found in Fig. 9 and using an ideal 90-degree hybrid device on the output side of the device instead of the IPP7048 to reduce phase distortion. It can be verified that under these conditions, the device is able to display the Doherty load impedance trajectory. The load impedance trajectories as input

power is swept from deep in OBO to saturation are displayed in Fig. 13. As shown, the load impedances go from twice the optimum at OBO, to the optimum at saturation, confirming Doherty behavior. The drain efficiency and gain across the power sweeps are displayed in Fig. 19, and clearly show Doherty-like efficiency curves, with peaks at saturation and 6 dB OBO.

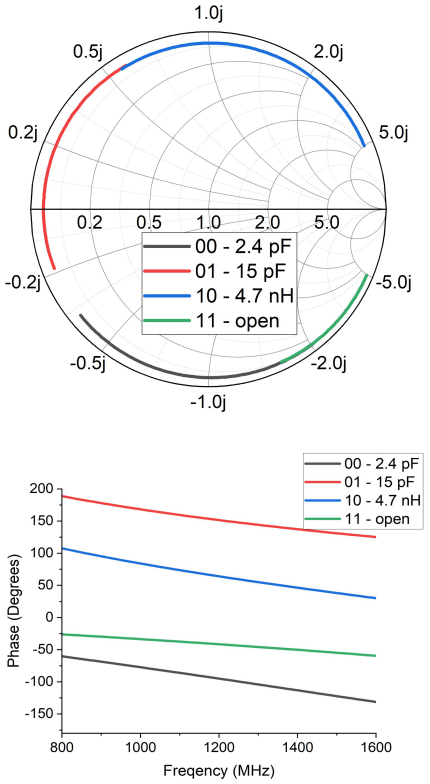

Fig. 14. Input reflection coefficient of the four reactive terminations and RF switch, over the 0.8–1.6 GHz band.

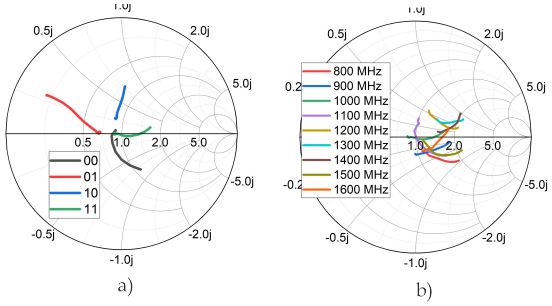

Fig. 15. a) Load trajectory at 1.0 GHz under each switch state condition. b) Load trajectory from 0.8 to 1.6 GHz with optimal switch state. Both charts are normalized to 12 Ω.

With Doherty behavior confirmed in the ideal case, the IPP7048 and the RF switch can be reintroduced. The switch's functionality is displayed in Fig. 15a). This shows four power sweeps at 1.0 GHz using the four different switch conditions. Here, only one condition provides proper load modulation for Doherty behavior, whereas the other three conditions are scattered orthogonally from each other. The best switch condition

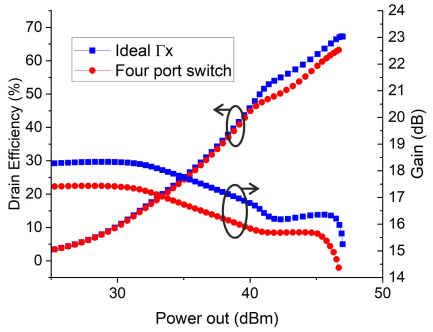

Fig. 16. Drain efficiency and gain at 1.2 GHz. The blue trace is with the ideal Γ_x and the red trace is with the RF switch using the "10" state (4.7 nH reactive termination).

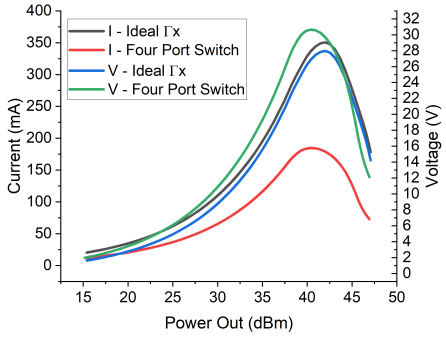

Fig. 17. Current and voltage incident at the isolated port both with the ideal Γ_x and with the four-port switch. Both plots are at 1.2 GHz.

can be found at each frequency point by repeating this sweep and identifying the condition that offers the best Doherty load trajectory. The Load trajectories with the identified Γ_x conditions are shown in Fig. 15 b). As expected, the load trajectories are more scattered when compared to the ideal case, but still close enough to Doherty behavior to ensure good OBO efficiency. Naturally, the device's performance degrades slightly as it is moved away from the idealized condition to a more realistic one. Fig. 16 shows a side-by-side comparison of the power sweep at 1.2 GHz using both the ideal Γ_x and the best switch conditions. Here, the gain drops by 0.9 dB beyond the 6 dB OBO region, which then reduces to 0.5 to 0.8 dB across the OBO region. Likewise, the drain efficiency drops by around 4% at OBO and at most 5.7 % across the OBO region. As previously stated, the magnitude of Γ_x is negligible, so the loss in performance is likely to be attributed to the fact that the phase of the Γ_x is no longer ideal; therefore, the load modulation is no longer optimal. Moreover, the current and voltage at the isolated port of the device are shown in Fig. 17. This confirmed that the switch is not in the direct power path at saturation as the current and voltage are at a maximum at the 6 dB OBO point and drop over the OBO region. The maximum power at the isolated port is around 25 dBm at the 6 dB OBO point with the RF switch.

Also, by inserting in (28) the values of maximum current and voltage from Fig. 17, it is possible to verify that the

theoretical calculation of the maximum of V_3 and I_3. The obtained values for P_{MAX} are $\simeq$48 W for the ideal Γ_x case, and $\simeq$36 W for the real switch case, not too far from the 40/50 W maximum output power expected from this design. This means that the simplified calculation of V_3 and I_3 is a good first approximation for assessing the maximum current and voltage on the reflective load. The overall schematic of the final design is shown in Fig. 18

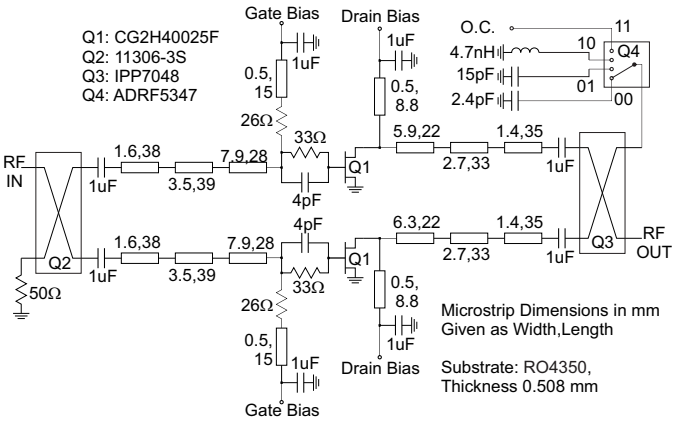

Fig. 18. Schematic diagram of the prototype, designed on RO4054B substrate with 508 μm thickness. Transmission line dimensions are in millimeters.

The results of power sweeps with the identified switch conditions are shown in Fig. 19, while a chart to compare the drain efficiency at saturation and OBO is shown in Fig. 20.

V. Experimental Characterization

A. Single-Tone Characterization

Fig. 21 shows a picture of the prototype, fabricated and assembled on an aluminum fixture with SMA launchers for the RF signals. As there was uncertainty about the ability of the switch to handle the signal applied, the initial test was done using a pulsed single-tone stimulus. The pulse width was set at 50 μs, with a duty cycle of 10%. Wideband power sensors were used to measure the power at the input and output ports, alongside a spectrum analyzer at the output to check the spectral content and make sure no oscillations were appearing. The current consumption was calculated by dividing the DC current, measured at the DC supply, by the duty cycle. The accuracy of such a measurement was verified by conducting some initial measurements with a current probe. The quiescent biasing condition for the experimental campaign is a drain voltage of 28 V for both devices, main drain current of 30 mA, and auxiliary gate voltage of -9 V.

Fig. 22 shows a collection of power sweep results at different tone frequencies over the target frequency bands. At each tone frequency, the switch is adjusted at the corresponding optimum state. Fig. 23 shows a summary of the performance vs. frequency. On the 0.8–1.6 GHz band, the maximum output power measured ranges between 45 and 47.3 dBm, while remaining above 46 dBm on the majority of the band except for 1.3 GHz, and the corresponding efficiency and PAE better than 63% and 52%, respectively. At 6 dB OBO, the efficiency

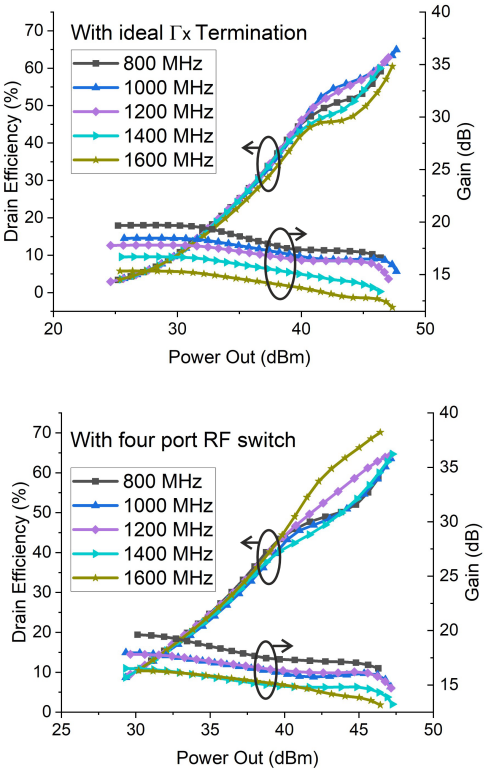

Fig. 19. Simulation gain and drain efficiency under both ideal Γ_x and using the four-port RF switch

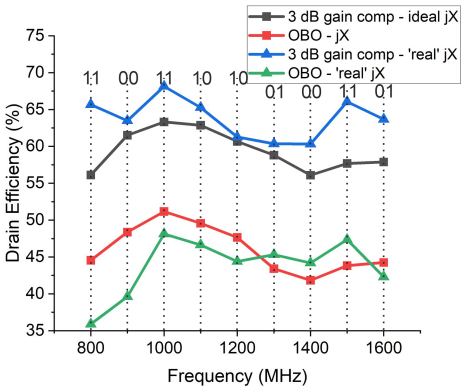

Fig. 20. Comparison of the optimal OBO and saturation efficiency at all frequencies with optimal switch condition

and PAE are higher than 48% and 43%, respectively, and the corresponding gain remains above 9.3 dB on the whole band.

The measured performance of the PA is compared with the State of the Art in Table I. The performance compares favorably with the state of the art, showing good output power over the band, with fair efficiency performance.

B. Modulated Signal Characterization

The system-level measurements were carried out using the Amplifier Testing tool from R&S that coordinates the signal source (SMW200A) and analyzer (FSW). Fig. 24 shows

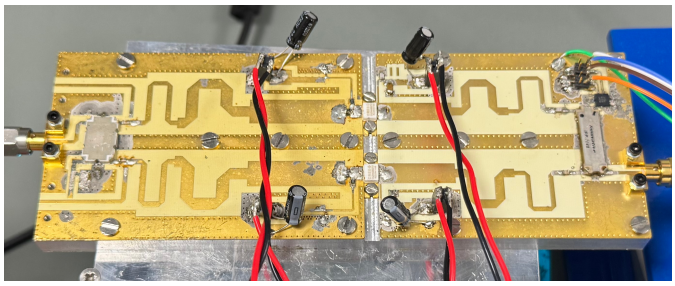

Fig. 21. Picture of the fabricated prototype. The device's dimensions are 169.2 mm x 60 mm

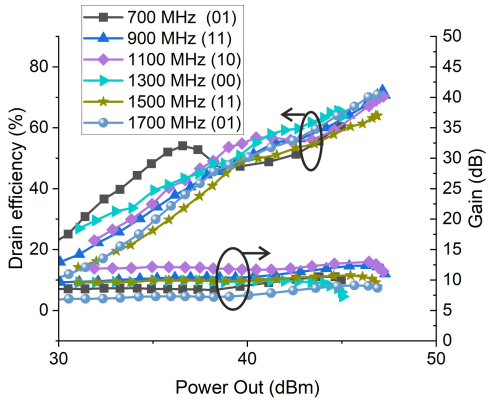

Fig. 22. Measured single-tone power sweeps results at different frequencies. Pulsed with 50 μs pulse width, 10% duty cycle. Efficiency and gain vs. output power.

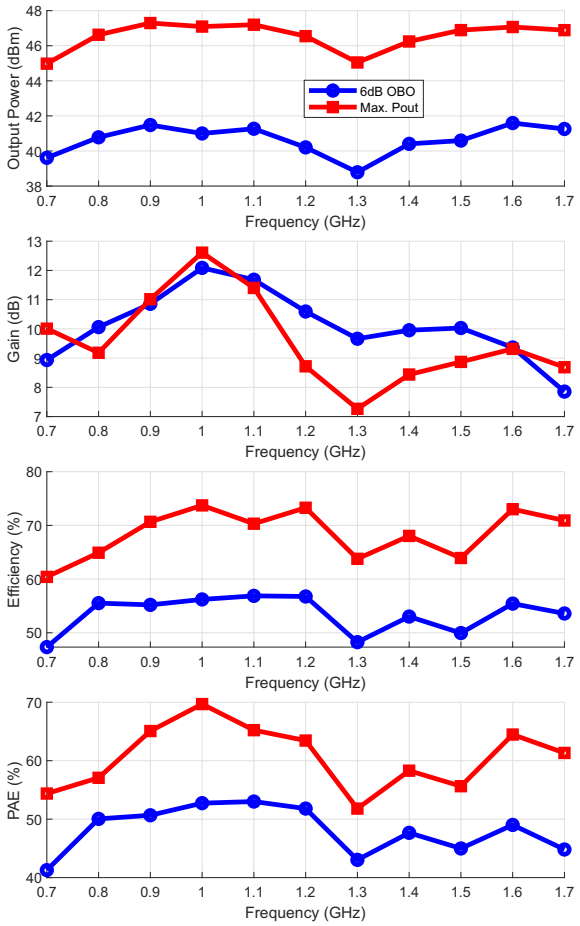

Fig. 23. Measured single-tone power sweeps results vs. frequency. Pulsed with 50 μs pulse width, 10% duty cycle. Output, gain, efficiency and PAE vs. frequency, at maximum power and at 6 dB OBO.

a picture of the measurement setup. The system was pre-calibrated using the S-parameters of several blocks so that an accurate power reading was available at the prototype's input and output. The system also records the DC currents for efficiency calculations.

The test signal applied is a multi-tone signal generated by the instrument, with 6-dB crest factor, and channel occupation of 5 MHz. The test was performed from 0.8 to 1.7 GHz with 100 MHz step using, at each frequency, the optimum reflective termination (switch condition) identified in simulations and verified in pulsed single-tone testing. Fig. 25 shows the output spectra at the different center frequencies. The average power was set, at each frequency, at the highest level that still allowed, with digital predistortion (DPD) applied, to achieve around -45 dBc of Adjacent Channel Leakage Ratio (ACLR). The DPD algorithm used is the direct DPD integrated within the R&S Amplifier Testing tool [30]. Fig. 26 summarizes the system level performance, showing the average power, efficiency, PAE and ACLR vs. center frequency, when the DPD is applied. From 0.8 to 1.7 GHz, the average output power is 41 dBm $\pm$ 1 dB, with ACLR better than -45 dBc. The corresponding average efficiency is higher than 38%, and the PAE is higher than 31%. The values are lower than what was measured with the pulsed single-tone characterization. On top of some uncertainty in the two measurements, we believe that the difference in the performance might be due to a better thermal condition in the pulsed measurements. Nonetheless,

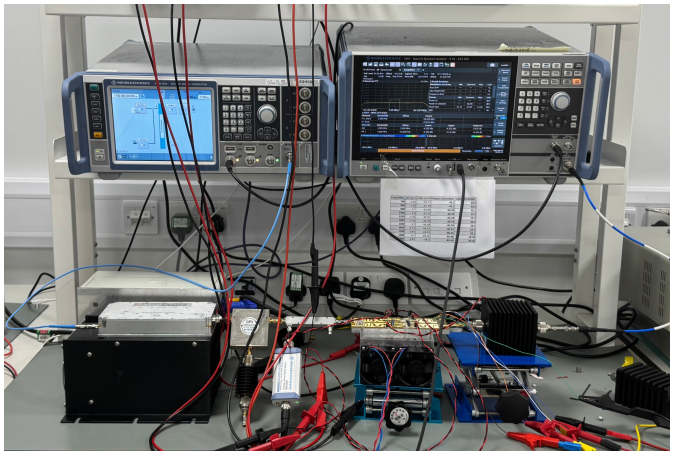

Fig. 24. Picture of the system level characterization setup.

the system-level results are still fairly good, and show the effectiveness of the new technique proposed in tuning the PA behavior for agile frequency operation.

VI. Conclusion

The paper has presented an exhaustive explanation of the mode of operation of the OLMBA in Doherty-like mode,

TABLE I
COMPARISON WITH STATE OF THE ART BROADBAND LMBAS AND DPAS.

Ref. Year	PA Type	Freq. (GHz)	RBW (%)	Pmax (dBm)	OBO (dB)	DE@OBO (%)
This	OLMBA	0.8–1.6	67	45–47.3	6	48–57
[19] 2025	PD-LMBA	0.2–2	164	44–45	10	44–62
[20] 2023	SLMBA	1.3–2.1	47	50.3–53	10	42–53
[28] 2022	SLMBA	1.8–2.75	42	44.6–45.8	6/8	51–63.8
[29] 2023	SLMBA	2.05–3.65	56	45.2–46.8	6/8	50.5–66.2
[14] 2018	LMBA	1.7–2.5	38	48–48.9	6/8	43–53
[16] 2020	CM-LMBA	1.45–2.45	51	45.6–46.7	6/8	51.2–64.4
[15] 2018	RF-LMBA	2.4	–	45.6	6	54
[26] 2021	QB-DPA	3.4–3.6	0.1	40.7	6	46.2–59.8
[6] 2018	DPA	1.35–2.05	41	41.5–42.4	9	52–55
[7] 2018	DPA	1.5–3.8	87	42.3–43.4	6	33-55
[25] 2013	DPA	1.9–2.3	15	41.5–42	6	48-50
[8] 2012	DPA	2.2–3.0	31	39.5–42	6	36-48
[9] 2021	DPA	1.4–2.5	56	42.9–44.8	6	44-60

highlighting the practical limitations and providing a recipe for its design. The experimental characterization of the first prototype showed the ability to tune the center frequency of operation by changing the state of a switch, achieving high average efficiency and uniform output power over an octave bandwidth. This new type of amplifier represents an alternative to broadband load modulated amplifiers, and further engineering and advancements can target a further increase of the RF bandwidth covered, and an expansion of the output back-off region of high efficiency.

APPENDIX A
MATCHING COUPLER EQUIVALENCE

Let's consider the schematic diagram of Fig. 27.

Let's assume that the 4-port network with scattering matrix $\mathbf{S}'$ represents an ideal, lossless quadrature 3-dB coupler:

$$\mathbf{S}' = \frac{1}{\sqrt{2}} \begin{bmatrix} 0 & 0 & +1 & -j \\ 0 & 0 & -j & +1 \\ +1 & -j & 0 & 0 \\ -j & +1 & 0 & 0 \end{bmatrix}, \tag{29}$$

with reference impedance Z_0 for all ports.

The 2-port networks connected to port 1 and 2, represented by the scattering matrix $\mathbf{S}_\mathrm{m}$, are identical lossless matching networks that transform Z_0 on the coupler side to R_opt on the input side, with an equivalent phase delay $\Delta\Phi$:

$$\mathbf{S}_\mathrm{m} = e^{-j\Delta\Phi} \begin{bmatrix} 0 & 1 \\ 1 & 0 \end{bmatrix}, \tag{30}$$

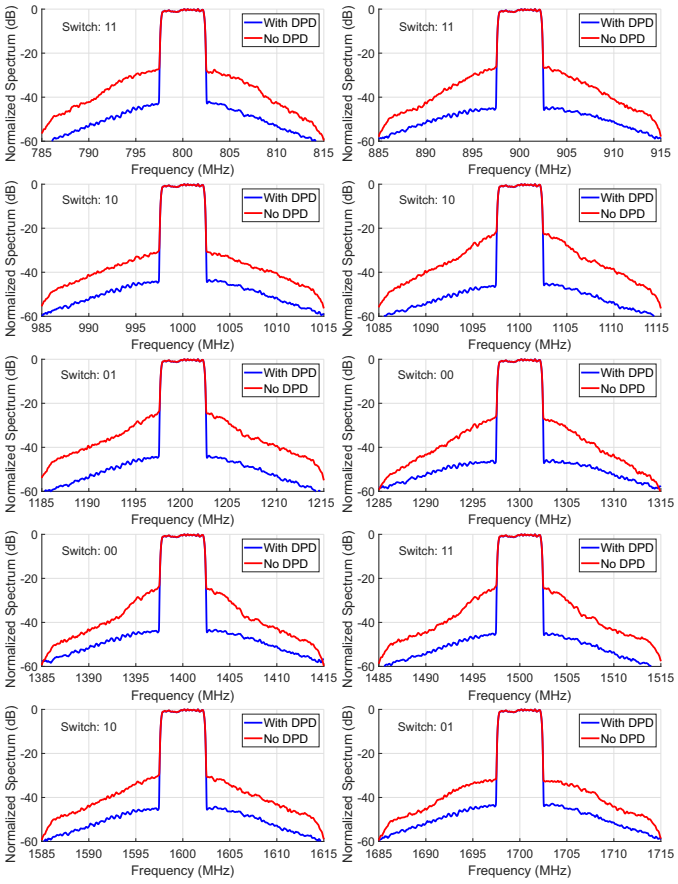

Fig. 25. Measured output spectra at different center frequencies, with 5 MHz channel, 6-dB PAPR test signal. Without (red) and with (blue) DPD applied.

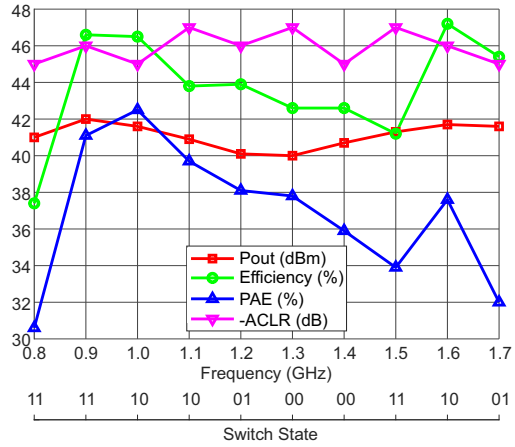

Fig. 26. Summary of system level performance with 5 MHz channel, 6-dB PAPR test signal, after applying the DPD algorithm. Average output power, average efficiency, average PAE and ACLR vs. centre frequency. The switch state utilized at each center frequency is indicated at the bottom.

with reference impedance R_opt at port 1, and Z_0 at port 2.

The 2-port networks connected to port 3 and 4, represented by the scattering matrix $\mathbf{S}_\mathrm{h}$, are identical delay lines of impedance Z_0 and phase delay $-\Delta\Phi$:

$$\mathbf{S}_\mathrm{h} = e^{+j\Delta\Phi} \begin{bmatrix} 0 & 1 \\ 1 & 0 \end{bmatrix}, \tag{31}$$

with reference impedance Z_0 at both ports.

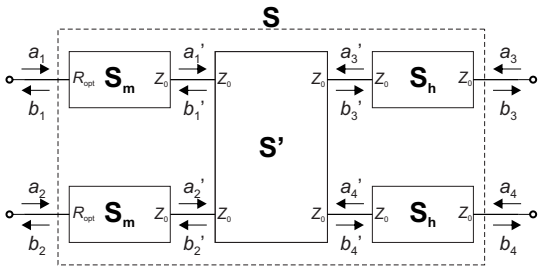

Fig. 27. Schematic diagram to support the demonstration of the equivalence of Fig. 3.

As the reference impedance at the interface between the 4-port network and the 2-port networks is always Z_0, the pseudo-waves at the interface are defined consistently so their relation is trivial.

This means that we can write the b waves as:

$$\begin{cases} b_1 = e^{-j\Delta\Phi} b_1' \\ b_2 = e^{-j\Delta\Phi} b_2' \\ b_3 = e^{+j\Delta\Phi} b_3' \\ b_4 = e^{+j\Delta\Phi} b_4' \end{cases}. \tag{32}$$

and the a' waves as:

$$\begin{cases} a_1' = e^{-j\Delta\Phi} a_1 \\ a_2' = e^{-j\Delta\Phi} a_2 \\ a_3' = e^{+j\Delta\Phi} a_3 \\ a_4' = e^{+j\Delta\Phi} a_4 \end{cases}. \tag{33}$$

As the b' waves can be written as function of the a' waves by using $\mathbf{S}'$, the identities of (32) can be rewritten as:

$$\begin{cases} b_1 = e^{-j\Delta\Phi} \frac{1}{\sqrt{2}} \left(+a_3' - j a_4'\right) \\ b_2 = e^{-j\Delta\Phi} \frac{1}{\sqrt{2}} \left(-j a_3' + a_4'\right) \\ b_3 = e^{+j\Delta\Phi} \frac{1}{\sqrt{2}} \left(+a_1' - j a_2'\right) \\ b_4 = e^{+j\Delta\Phi} \frac{1}{\sqrt{2}} \left(-j a_1' + a_2'\right) \end{cases}. \tag{34}$$

Finally, by inserting (33) in (34):

$$\begin{cases} b_1 = e^{-j\Delta\Phi} \frac{1}{\sqrt{2}} \left(+a_3 - j a_4\right) e^{+j\Delta\Phi} = \frac{1}{\sqrt{2}} \left(+a_3 - j a_4\right) \\ b_2 = e^{-j\Delta\Phi} \frac{1}{\sqrt{2}} \left(-j a_3' + a_4'\right) e^{+j\Delta\Phi} = \frac{1}{\sqrt{2}} \left(-j a_3 + a_4\right) \\ b_3 = e^{+j\Delta\Phi} \frac{1}{\sqrt{2}} \left(+a_1 - j a_2\right) e^{-j\Delta\Phi} = \frac{1}{\sqrt{2}} \left(+a_1 - j a_2\right) \\ b_4 = e^{+j\Delta\Phi} \frac{1}{\sqrt{2}} \left(-j a_1 + a_2\right) e^{-j\Delta\Phi} = \frac{1}{\sqrt{2}} \left(-j a_1 + a_2\right) \end{cases}, \tag{35}$$

which means that the scattering matrix of the overall structure is:

$$\mathbf{S} = \frac{1}{\sqrt{2}} \begin{bmatrix} 0 & 0 & +1 & -j \\ 0 & 0 & -j & +1 \\ +1 & -j & 0 & 0 \\ -j & +1 & 0 & 0 \end{bmatrix}, \tag{36}$$

with reference impedance R_{opt} at port 1 and 2, and Z_0 at port 3 and 4.

REFERENCES

[1] D. Mikrut, P. Roblin, H.-C. Chang, S. Smith, J. Coffey, R. Tantawy, and D. Frey, "A brief overview of reconfigurable PA technologies : (invited paper)," in *IEEE Wireless and Microwave Technology Conference (WAMICON)*, Apr. 2024, pp. 1–4.

[2] A. Grebennikov and S. Bulja, "High-Efficiency Doherty Power Amplifiers: Historical Aspect and Modern Trends," *Proc. IEEE*, vol. 100, no. 12, pp. 3190 –3219, Dec. 2012.

[3] V. Camarchia, M. Pirola, R. Quaglia, S. Jee, Y. Cho, and B. Kim, "The Doherty power amplifier: Review of recent solutions and trends," *IEEE Trans. Microw. Theory Techn.*, vol. 63, no. 2, pp. 559–571, Feb. 2015.

[4] R. Quaglia, M. Pirola, and C. Ramella, "Offset lines in Doherty power amplifiers: Analytical demonstration and design," *IEEE Microw. Wireless Compon. Lett.*, vol. 23, no. 2, pp. 93 –95, Feb. 2013.

[5] K. Bathich, A. Markos, and G. Boeck, "Frequency response analysis and bandwidth extension of the Doherty amplifier," *IEEE Trans. Microw. Theory Techn.*, vol. 59, no. 4, pp. 934 –944, Apr. 2011.

[6] X.-H. Fang, H.-Y. Liu, K.-K. M. Cheng, and S. Boumaiza, "Modified Doherty amplifier with extended bandwidth and back-off power range using optimized peak combining current ratio," *IEEE Trans. Microw. Theory Techn.*, vol. 66, no. 12, pp. 5347–5357, Dec. 2018.

[7] J. J. M. Rubio, V. Camarchia, M. Pirola, and R. Quaglia, "Design of an 87% fractional bandwidth Doherty power amplifier supported by a simplified bandwidth estimation method," *IEEE Trans. Microw. Theory Techn.*, vol. 66, no. 3, pp. 1319–1327, Mar. 2018.

[8] G. Sun and R. H. Jansen, "Broadband Doherty power amplifier via real frequency technique," *IEEE Trans. Microw. Theory Techn.*, vol. 60, no. 1, pp. 99–111, Jan. 2012.

[9] C. Liang, J. I. Martinez-Lopez, P. Roblin, Y. Hahn, D. Mikrut, and V. Chen, "Wideband two-way hybrid Doherty outphasing power amplifier," *IEEE Trans. Microw. Theory Techn.*, vol. 69, no. 2, pp. 1415–1428, Feb. 2021.

[10] G. Bartolotti, A. Piacibello, and V. Camarchia, "Integrated 5-W GaN Doherty power amplifier for 5G FR1 bands with 19 dB gain over a 41% bandwidth," in *IEEE/MTT-S International Microwave Symposium - IMS 2024*, June 2024, pp. 378–381.

[11] A. M. M. Mohamed, S. Boumaiza, and R. R. Mansour, "Electronically tunable Doherty power amplifier for multi-mode multi-band base stations," *IEEE Trans. Circuits Syst. I, Reg. Papers*, vol. 61, no. 4, pp. 1229–1240, Apr. 2014.

[12] J. Pang, Z. Dai, Y. Li, M. Li, and A. Zhu, "Multiband dual-mode Doherty power amplifier employing phase periodic matching network and reciprocal gate bias for 5G applications," *IEEE Trans. Microw. Theory Techn.*, vol. 68, no. 6, pp. 2382–2397, June 2020.

[13] D. J. Shepphard, J. Powell, and S. C. Cripps, "An efficient broadband reconfigurable power amplifier using active load modulation," *IEEE Microw. Wireless Compon. Lett.*, vol. 26, no. 6, pp. 443–445, Jun. 2016.

[14] R. Quaglia and S. Cripps, "A load modulated balanced amplifier for telecom applications," *IEEE Trans. Microw. Theory Techn.*, vol. 66, no. 3, pp. 1328–1338, Mar. 2018.

[15] P. H. Pednekar, W. Hallberg, C. Fager, and T. W. Barton, "Analysis and design of a Doherty-like RF-input load modulated balanced amplifier," *IEEE Trans. Microw. Theory Techn.*, vol. 66, no. 12, pp. 5322–5335, Dec. 2018.

[16] J. Pang, C. Chu, Y. Li, and A. Zhu, "Broadband RF-input continuous-mode load-modulated balanced power amplifier with input phase adjustment," *IEEE Trans. Microw. Theory Techn.*, vol. 68, no. 10, pp. 4466–4478, Oct. 2020.

[17] J. Pang, Z. Dai, Y. Li, M. Li, and A. Zhu, "Multiband dual-mode Doherty power amplifier employing phase periodic matching network and reciprocal gate bias for 5G applications," *IEEE Trans. Microw. Theory Techn.*, vol. 68, no. 6, pp. 2382–2397, June 2020.

[18] K. Chaudhry, R. Quaglia, and S. Cripps, "A load modulated balanced amplifier with linear gain response and wide high-efficiency output power back-off region," in *International Workshop on Integrated Nonlinear Microwave and Millimetre-Wave Circuits (INMMiC)*, Apr. 2020, pp. 1–3.
[19] P. Gong, J. Guo, N. B. Vangipurapu, and K. Chen, "Signal-flow-based analysis and design of pseudo-doherty load-modulated balanced amplifier toward unlimited rf bandwidth," *IEEE Trans. Microw. Theory Techn.*, vol. 73, no. 1, pp. 206–220, Jan. 2025.
[20] C. Belchior, L. C. Nunes, P. M. Cabral, and J. C. Pedro, "Sequential LMBA design technique for improved bandwidth considering the balanced amplifiers off-state impedance," *IEEE Trans. Microw. Theory Techn.*, vol. 71, no. 8, pp. 3629–3643, Aug. 2023.
[21] D. J. Collins, R. Quaglia, J. R. Powell, and S. C. Cripps, "The orthogonal LMBA: A novel RFPA architecture with broadband reconfigurability," *IEEE Microw. Wireless Compon. Lett.*, vol. 30, no. 9, pp. 888–891, Sep. 2020.
[22] R. Quaglia, J. R. Powell, K. A. Chaudhry, and S. C. Cripps, "Mitigation of load mismatch effects using an orthogonal load modulated balanced amplifier," *IEEE Trans. Microw. Theory Techn.*, vol. 70, no. 6, pp. 3329–3341, June 2022.
[23] J.-B. Urvoy, R. Quaglia, J. R. Powell, and S. C. Cripps, "Experimental characterization of a dual-input OLMBA for back-off efficiency improvement," in *53rd European Microwave Conference (EuMC)*, Sep. 2023, pp. 267–270.
[24] J.-B. Urvoy, R. Quaglia, and S. C. Cripps, "Design and simulation of a Doherty-mode OLMBA for enhanced back-off efficiency over an octave bandwidth," in *International Workshop on Integrated Nonlinear Microwave and Millimetre-Wave Circuits (INMMIC)*, Apr. 2025, pp. 1–4.
[25] R. Giofré, L. Piazzon, P. Colantonio, and F. Giannini, "A Doherty architecture with high feasibility and defined bandwidth behavior," *IEEE Trans. Microw. Theory Techn.*, vol. 61, no. 9, pp. 3308–3317, Sep. 2013.
[26] H. Lyu, Y. Cao, and K. Chen, "Linearity-enhanced quasi-balanced Doherty power amplifier with mismatch resilience through series/parallel reconfiguration for massive MIMO," *IEEE Trans. Microw. Theory Techn.*, vol. 69, no. 4, pp. 2319–2335, Apr. 2021.
[27] S. U. Ghozati, R. Quaglia, E. Azad, J. Powell, P. Tasker, and S. Cripps, "Load pull-driven behavioral modelling of microwave switches for the design of tunable reflective terminations," in *18th European Microwave Integrated Circuits Conference (EuMIC)*, Sep. 2023, pp. 1–4.
[28] C. Chu, T. Sharma, S. K. Dhar, R. Darraji, X. Wang, J. Pang, and A. Zhu, "Waveform engineered sequential load modulated balanced amplifier with continuous class–F-1 and class–J operation," *IEEE Trans. Microw. Theory Techn.*, vol. 70, no. 2, pp. 1269–1283, Feb. 2022.
[29] C. Chu, J. Pang, R. Darraji, S. K. Dhar, T. Sharma, and A. Zhu, "Broadband sequential load modulated balanced amplifier with extended design space using second harmonic manipulation," *IEEE Trans. Microw. Theory Techn.*, vol. 71, no. 5, pp. 1990–2003, May 2023.
[30] Rhode and Schwarz, "Iterative direct dpd white paper [online]." [Online]. Available: https://scdn.rohde-schwarz.com/ur/pws/dl_downloads/dl_application/application_notes/1ef99/1EF99_Iterative_Direct_DPD_1e.pdf

Jean-Baptiste Urvoy received his MEng from Cardiff University in 2022. He is currently pursuing a PhD with the Centre for High Frequency Engineering (CHFE) at Cardiff University. His research interests include the design of power amplifiers for reconfigurable multi-mode and multi-frequency applications.

Ehsan M. Azad received his bachelor's degree in petroleum engineering from the University of Gachsaran, Iran, in 2012. Following this, he pursued his interest in electronics by completing a college degree from Cardiff and Vale College, UK, in 2018. Subsequently, he earned both his M.Sc. degree in wireless and microwave communication engineering and his Ph.D. degree in efficiency improvement of base station power amplifiers from the Centre for High Frequency Engineering (CHFE) at Cardiff University, UK, in 2019 and 2023, respectively. Since October 2022, he has been part of CSA Catapult, UK, contributing to collaborative projects focused on the development of millimeter-wave power amplifiers (PAs). His research interests include various areas, including high-efficiency PAs, with a particular emphasis on Doherty PAs, nonlinear device characterization and modeling, PA linearization techniques, and advanced packaging solutions.

Aleksander Bogusz received MEng and PhD degrees from the School of Engineering at Cardiff University, Wales, UK, in 2012 and 2022, respectively. He works as a Research Associate at the Centre for High Frequency Engineering at Cardiff University. Additionally, he is a Senior Research Fellow at the Compound Semiconductor Applications Catapult, Newport, UK, where he focuses on the nonlinear modelling of III-V semiconductor devices. His research interests include the design and characterisation of efficient broadband power amplifiers, efficiency enhancement techniques, and instrumentation for microwave and mm-wave applications. Dr Bogusz serves on the IEEE MTT-S Technical Committee on Microwave High-Power Techniques (TC-12).

Prof. Steve Cripps (M'81-SM'90-F'11-LF'16) received the master's and Ph.D. degrees from Cambridge University, Cambridge, U.K., in 1975. He spent many years working within the high frequency ("microwave") electronics industry in the U.K. and the USA. He was a Designer, a Manager, and an Independent Consultant. He is currently a Distinguished Research Professor with Cardiff University, Wales, U.K. He has authored several books on RF Power Amplifiers. Dr. Cripps was a recipient of the 2008 IEEE Microwave Applications Award and the 2015 Microwave Prize. He served as an Associate Editor for IEEE MICROWAVE AND WIRELESS COMPONENTS LETTERS.

Roberto Quaglia was born in Casale Monferrato, Italy, in 1984. He graduated *cum laude* in electronic engineering from Politecnico di Torino in 2008. In 2012, he received the Ph.D. degree in electronic devices from the Politecnico di Torino, Turin, Italy. His research interests concern the design, modeling and predistortion of high efficiency MMIC power amplifiers, and he is currently a Senior Lecturer at the School of Engineering of Cardiff University. He is a member of the IEEE MTT-TC 12. Dr. Quaglia was the recipient of a European Union Marie Skłodowska Curie fellowship in 2015, and of the 2009 Young Graduated Research Fellowship presented by the GAAS Association.